

# Geometric Amplitude Accompanying Local Responses: Spinor Phase Information from the Amplitudes of Spin-Polarized STM Measurements

Shu-Hui Zhang<sup>1,\*</sup>, Jin Yang,<sup>2</sup> Ding-Fu Shao<sup>3</sup>, Jia-Ji Zhu,<sup>4</sup> Wen Yang,<sup>2,†</sup> and Kai Chang<sup>5,6,‡</sup>

<sup>1</sup>College of Mathematics and Physics, Beijing University of Chemical Technology, Beijing 100029, China

<sup>2</sup>Beijing Computational Science Research Center, Beijing 100193, China

<sup>3</sup>Key Laboratory of Materials Physics, Institute of Solid State Physics, HFIPS, Chinese Academy of Sciences, Hefei 230031, China

<sup>4</sup>School of Science, Chongqing University of Posts and Telecommunications, Chongqing 400061, China

<sup>5</sup>Center for Quantum Matter, School of Physics, Zhejiang University, Hangzhou 310027, China

<sup>6</sup>Institute for Advanced Study in Physics, Zhejiang University, Hangzhou 310027, China

 (Received 24 July 2023; revised 30 January 2024; accepted 11 June 2024; published 19 July 2024)

Solving the Hamiltonian of a system yields the energy dispersion and eigenstates. The geometric phase of the eigenstates generates many novel effects and potential applications. However, the geometric properties of the energy dispersion go unheeded. Here, we provide geometric insight into energy dispersion and introduce a geometric amplitude, namely, the geometric density of states (GDOS) determined by the Riemann curvature of the constant-energy contour. The geometric amplitude should accompany various local responses, which are generally formulated by the real-space Green's function. Under the stationary phase approximation, the GDOS simplifies the Green's function into its ultimate form. In particular, the amplitude factor embodies the spinor phase information of the eigenstates, favoring the extraction of the spin texture for topological surface states under an in-plane magnetic field through spin-polarized STM measurements. This work opens a new avenue for exploring the geometric properties of electronic structures and excavates the unexplored potential of spin-polarized STM measurements to probe the spinor phase information of eigenstates from their amplitudes.

DOI: [10.1103/PhysRevLett.133.036204](https://doi.org/10.1103/PhysRevLett.133.036204)

*Introduction*—A quantum system is described by a Hamiltonian. Solving the Hamiltonian is a prerequisite for exploring the properties of a system and generating the energy dispersion and eigenstates that underlie the electronic band theory for crystalline materials [1]. In conventional cognition, energy dispersion controls the physical properties of crystalline materials [2], whereas the eigenstates are not valued until the accompanying geometric phase is identified [3,4]. The geometric phase has become an essential component of modern band structure theory and generates various remarkable phenomena [5]. However, the geometric properties of energy dispersion are unexplored.

Macroscopic and global measurements are typically used to reveal phenomena originating from the geometric phase [6]. Conversely, local measurements are likely to reflect the local information of crystalline materials, which is required for a low-dimensional system [7,8]. There are emergent nonmagnetic, magnetic, topological two-dimensional (2D) materials and exotic surface states of three-dimensional topological insulators and semimetals, their novel physics and potential applications [9–15] promote the continuously increasing demand for local information. Recently, two

experiments used scanning tunneling microscopy (STM) to measure the Friedel oscillation or quasiparticle interference (QPI) in real space [16] induced by intentionally introduced single impurity, and then identified the Berry phases of monolayer and bilayer graphene [17,18]. The two experiments were performed on a multiple-valley system, i.e., graphene as the model system without spin-orbit coupling. However, these are not applicable to a single-valley system, e.g., the surface states of a three-dimensional topological insulator (TISS) as the model system with spin-orbit coupling. The success of the two experiments [17,18] inspired us to identify electronic information with higher complexity in local responses.

In this study, we provide geometric insight into the energy dispersion, and consider the constant-energy contour (CEC) as a geometric entity. The Riemann curvature of the CEC microscopically determines the density of states (DOS), which is then called geometric DOS (GDOS). The GDOS represents a type of geometric amplitude, unlike the well-known geometric phase [5]. The GDOS governs the amplitude of the real-space Green's function (GF) under the stationary phase approximation and enables it to attain the ultimate expression in which each factor corresponds to specific electronic information. The GDOS should be accompanied by various local responses, which are generally formulated by the GF. As an example, we propose characterizing the spin texture of a TISS under an in-plane magnetic field [19–21] using the spin-polarized

\*Contact author: shuhuizhang@mail.buct.edu.cn

†Contact author: wenyang@csrc.ac.cn

‡Contact author: kchang@zju.edu.cn

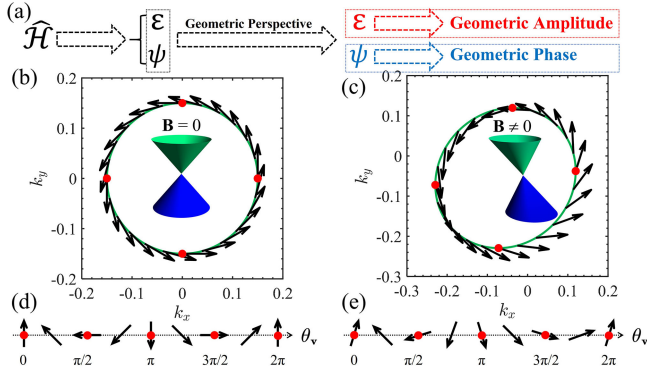


FIG. 1. (a) Solving the system Hamiltonian  $\hat{\mathcal{H}}$  yields the energy dispersion  $\varepsilon$  and eigenstates  $\psi$  (colored by the geometric perspective). These generate the geometric amplitude and geometric phase, respectively. (b), (c) Schematic circular and elliptical constant-energy contours (fringed by the spin texture, black arrows) of the untilted and tilted Dirac cones (insets) corresponding to the surface states of the topological insulator for  $\mathbf{B} = 0$  and  $\mathbf{B} \neq 0$ . Here,  $\mathbf{B}$  is an in-plane magnetic field. (d), (e) The spin vectors rotate periodically with the azimuthal angle  $\theta_v$  of the group velocity along the circular and elliptical constant-energy contours.

STM measurements in real space. This study complements the geometric perspective of the Hamiltonian or the corresponding electronic structure [cf. Fig. 1(a)]. Therefore, the GDOS is fundamental and powerful to explore crystalline materials and other periodic systems.

*Model*—We consider the TISS under an in-plane magnetic field. It has recently attracted significant interest because of its novel effects, such as the planar Hall effect [19,20,22] and super-resonant transport [21]. The TISS under an in-plane magnetic field can be described by the Hamiltonian [19,21,23]

$$\mathcal{H}(\mathbf{k}) = v_F(k_x\sigma_y - k_y\sigma_x) + \mathbf{t} \cdot \mathbf{k}, \quad (1)$$

where  $\mathbf{k} = (k_x, k_y)$  is the momentum,  $\sigma_{x,y}$  are Pauli matrices for the spin vector  $\boldsymbol{\sigma}$ ,  $v_F$  is the velocity parameter, and  $\mathbf{t} = (t_x, t_y)$  is the tilt vector induced by the applied in-plane magnetic field  $\mathbf{B}$  [19,21]. The corresponding energy dispersion and eigenstates are  $E_{\eta,\mathbf{k}} = t_x k_x + t_y k_y + \eta v_F k$  and  $|u_\eta(\mathbf{k})\rangle = 1/\sqrt{2}[1\eta e^{i\Theta_{\mathbf{k}}}]^T$ , respectively. Here,  $\eta = \pm$  for the conductance and valence bands.  $\Theta_{\mathbf{k}} = \arg(k_y - ik_x)$  is the spinor phase of eigenstates, which determines the orientation of the spin vector because  $\langle u_\eta(\mathbf{k})|\boldsymbol{\sigma}|u_\eta(\mathbf{k})\rangle = \eta(\cos\Theta_{\mathbf{k}}, \sin\Theta_{\mathbf{k}})$ . The in-plane magnetic field tilts the Dirac cone of the TISS by comparing the electronic structures at  $\mathbf{B} = \mathbf{0}$  [cf. inset of Fig. 1(b)] and  $\mathbf{B} \neq \mathbf{0}$  [cf. inset of Fig. 1(c)]. In Figs. 1(b) and 1(c), the CECs are fringed by spin vectors, namely, the spin texture.

*Geometric density of states and the ultimate Green's function*—To characterize the spin texture of the TISS, we propose the experimental setup shown in Fig. 2(a), i.e., probing the QPI in real space induced by the designed

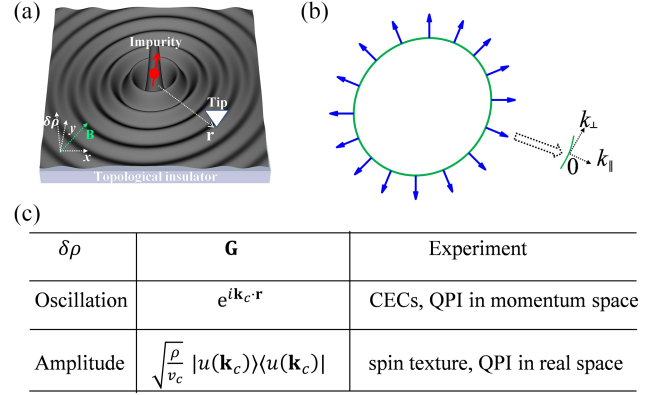


FIG. 2. (a) For the surface states (black) on the three-dimensional topological insulator (light blue), a single magnetic impurity (red dot) at  $\mathbf{r} = 0$  is introduced intentionally. The impurity-induced quasiparticle interference in real space  $\delta\rho$  (black oscillation waves) can be measured by spin-polarized scanning tunneling microscopy with the tip at  $r \neq 0$  (white triangle), even under an in-plane magnetic field  $\mathbf{B}$ . The inset shows the coordinate system with  $\mathbf{B}$  lying in the  $x$ - $y$  plane. (b) A general elliptical constant-energy contour fringed by the texture of group velocity  $\mathbf{v}$ .  $\mathbf{v}$  defines the unit vectors  $\mathbf{n}_{\parallel} = \mathbf{v}/|\mathbf{v}|$  and  $\mathbf{n}_{\perp} = \mathbf{z} \times \mathbf{v}/|\mathbf{v}|$ .  $\mathbf{z}$  is directed away from the plane. The enlarged inset shows a local coordinate system  $k_{\parallel} - k_{\perp}$  constructed using  $k_{\parallel} = \mathbf{k} \cdot \mathbf{n}_{\parallel}$  and  $k_{\perp} = \mathbf{k} \cdot \mathbf{n}_{\perp}$ . (c) The oscillation and the amplitude of  $\delta\rho$  originate from corresponding factors of the Green's function  $\mathbf{G}$ . These are exploited to determine the constant-energy contour by conventional quasiparticle interference in momentum space and the spin texture by quasiparticle interference in real space, as proposed in the main text.

magnetic impurity using spin-polarized STM. The in-plane magnetic field breaks the time-reversal symmetry of the TISS and causes the elliptical CEC to lose its inversion symmetry in the momentum space [cf. Fig. 1(c)]. In local responses, the spin-velocity locking (but not the spin-momentum locking) is the contributing mechanism [cf. Figs. 1(d) and 1(e) for the periodically rotating spin vectors with the angle  $\theta_v$  of the group velocity along the circular and elliptical CECs] [34]. In Fig. 2(b), the velocity texture is fringed on the CEC. In particular, the velocity vector defines a local coordinate system  $k_{\parallel} - k_{\perp}$  through  $k_{\parallel} = \mathbf{k} \cdot \mathbf{n}_{\parallel}$  and  $k_{\perp} = \mathbf{k} \cdot \mathbf{n}_{\perp}$  by using  $\mathbf{n}_{\parallel} = \mathbf{v}/|\mathbf{v}|$  and  $\mathbf{n}_{\perp} = \mathbf{z} \times \mathbf{v}/|\mathbf{v}|$  (shown in the inset). Here, the group velocity is  $\mathbf{v} = \nabla_{\mathbf{k}} E_{\eta\mathbf{k}}$ . For the CEC, there is a textbook concept as a shortcut to capture the effective information from the electronic structure [35], namely, the DOS, which is defined as  $\rho_0(\varepsilon) \equiv \delta N/\delta\varepsilon$  [1] with  $\delta N$  being the number of states in the energy range  $\delta\varepsilon$ . Analogous to  $\rho_0(\varepsilon)$ , we introduce the microscopic DOS  $\rho(\varepsilon, \theta_v) \equiv \delta N/(\delta\varepsilon\delta\theta_v)$ . From the inset of Fig. 2(b), we arrive at

$$\rho(\varepsilon, \theta_v) = \frac{1}{4\pi^2} \frac{\delta k_{\parallel} \delta s}{\delta\varepsilon \delta\theta_v} = \frac{1}{4\pi^2 v_{\mathbf{k}}}, \quad (2)$$

owing to the magnitude of the group velocity  $v = \delta\varepsilon/\delta k_{\parallel}$  and the curvature of the CEC  $\kappa = \delta\theta_v/\delta s$  with  $\delta s$  being the curve length of the CEC.  $\rho(\varepsilon, \theta_v)$  is determined by the Riemann curvature  $\kappa$ . Therefore, it attains the term GDOS. There are two implications for Eq. (2). It enables the straightforward calculation of the GDOS because  $\kappa$  is a well-known mathematical quantity [23,36] and enables the direct measurement of  $\kappa$  experimentally.

The GDOS enters the amplitude of the GF as the theoretical basis for local responses [37]. Under the stationary phase approximation, the GF arrives at the form [23]

$$\mathbf{g}(\varepsilon, \mathbf{r}) \approx -ie^{i\mathbf{k}_c \cdot \mathbf{r} - i\pi/4} \sqrt{\frac{2\pi\rho}{v_c r}} |u(\mathbf{k}_c)\rangle \langle u(\mathbf{k}_c)|, \quad (3)$$

where  $\mathbf{k}_c = (k_{x,c}, k_{y,c})$  is the stationary momentum on the CEC, and  $v_c = |\mathbf{v}_c|$  with  $\mathbf{v}_c$  as the group velocity at  $\mathbf{k}_c$ . For brevity, a single stationary momentum is considered in Eq. (3), while the summation over multiple stationary momenta is generally required [23]. For  $\mathbf{g}(\varepsilon, \mathbf{r})$ , except the constant factor  $-ie^{-i\pi/4}\sqrt{2\pi}$ , each of its factors corresponds to the specific electronic information. It is summarized by four features: (I) The oscillation wavelength of the GF depends on the Fermi wave vector  $\mathbf{k}_c$  in the exponential function [37]. (II) The GF decays following the dimension-determined power rate  $1/\sqrt{r} = 1/r^{(d-1)/2}$  with  $d = 2$  for 2D systems [38]. (III) The spinor eigenstate  $|u(\mathbf{k}_c)\rangle$  controls the matrix form of the GF through  $|u(\mathbf{k}_c)\rangle \langle u(\mathbf{k}_c)|$ . (IV) The amplitude is proportional to  $\sqrt{\rho}/v_c$  with  $\rho$  and  $v_c$  originating from the multimode property of 2D systems and the current normalization of eigenstates, respectively.

Figure 2(c) shows the usefulness of four features of GF. Experimentally, feature (I) is exploited in the conventional QPI in the momentum space, which can indirectly characterize the electronic structure [7,39–41]. Our ultimate physical expression of the real-space GF favors the straightforward simulation of QPI in real space, deserving the development of the relevant numerical package in future work. More importantly, feature (II) of the GF can be scaled out, leaving features (III) and (IV) into the amplitude of the QPI in real space which can be exploited to probe the spinor phase of eigenstates or spin texture [cf. Fig. 2(c)] as illustrated below.

*Characterization of spin texture by spin-polarized STM*—The spin texture of the TISS is extracted using the standard  $T$ -matrix approach [23,42], giving the QPI in real space characterized by the change of the local DOS [43,44]:

$$\delta Q_{\alpha\beta}(\varepsilon, \mathbf{r}) = -\frac{1}{\pi} \text{ImTr}[\mathbf{g}(\varepsilon, \mathbf{r}) \mathbf{T}_{\alpha} \mathbf{g}(\varepsilon, -\mathbf{r}) \sigma_{\beta}], \quad (4)$$

where the  $T$  matrix is expressed as

$$\mathbf{T}_{\alpha}(\varepsilon) = \mathbf{V}_{\alpha} [1 - \mathbf{g}(\varepsilon, \mathbf{0}) \mathbf{V}_{\alpha}]^{-1}, \quad (5)$$

where  $\mathbf{V}_{\alpha}$  represents the magnetic impurity potential. Here, we use the subscript  $\alpha \in \{0, x, y, z\}$  with  $\alpha = 0$  and  $\alpha \neq 0$  for the spin-unpolarized and spin-polarized imperfection or STM tip, respectively. Thus,  $\delta Q_{\alpha\beta}(\varepsilon, \mathbf{r})$  provides a  $\beta$ -resolved QPI induced by an  $\alpha$ -resolved imperfection. The real-space GF is necessary to analyze  $\delta Q_{\alpha\beta}(\varepsilon, \mathbf{r})$ , which is generally difficult to derive for the model Hamiltonian [45] and time-consuming to calculate for the first-principles electronic structure [46]. However, the ultimate expression of the GF, i.e., Eq. (3), can be derived conveniently after the CEC is specified. Utilizing Eq. (3) for the Hamiltonian in Eq. (1), we first derive the stationary points  $\mathbf{k}_c = (k_{x,c}, k_{y,c})$ . To consider the Fermi level in the conduction band, the group velocity is  $\mathbf{v} = (v_x, v_y)$  with  $v_{x,y} = t_{x,y} + v_F k_{x,y}/k$ . On the stationary points,  $\mathbf{v} \parallel \mathbf{r}$ , so  $v_y/v_x = \tan \theta_{\mathbf{r}}$  which gives the equation for  $\mathbf{k}$ . Combining the energy dispersion  $E_{+, \mathbf{k}} = \varepsilon$  for the given Fermi level  $\varepsilon$ , we obtain

$$k_{x,c}(\theta_{\mathbf{r}}) = \frac{\varepsilon}{v_F^2 v_m} [t_x t_y \sin \theta_{\mathbf{r}} + (v_F^2 - t_y^2) \cos \theta_{\mathbf{r}} - v_m t_x] \quad (6a)$$

$$k_{y,c}(\theta_{\mathbf{r}}) = \frac{\varepsilon}{v_F^2 v_m} [t_x t_y \cos \theta_{\mathbf{r}} + (v_F^2 - t_x^2) \sin \theta_{\mathbf{r}} - v_m t_y], \quad (6b)$$

where  $v_m = \sqrt{v_F^2 - t^2 \sin^2(\phi - \theta_{\mathbf{r}})}$  with  $\phi = \arg(t_x + it_y)$ , and  $v_F^2 = (v_F^2 - t_x^2 - t_y^2)$ . Then, one can obtain the classic velocity  $\mathbf{v}_c(\mathbf{r})$  and then its magnitude  $v_c = |\mathbf{v}_c| = t \cos(\theta_{\mathbf{r}} - \phi) + v_m$ . In addition, the curvature of the CEC corresponding to the energy dispersion is  $\kappa(\theta_{\mathbf{r}}) = v_m^3/(\varepsilon v_F^2)$ . According to Eq. (3), the explicit expression of the GF is

$$\mathbf{g}(\varepsilon, \pm \mathbf{r}) = c_{\pm} e^{i\mathbf{k}_{c,\pm} \cdot \mathbf{r}} \begin{bmatrix} 1 & e^{-i\Theta_{\pm}} \\ e^{i\Theta_{\pm}} & 1 \end{bmatrix}, \quad (7)$$

where  $c_{\pm} = -ie^{-i\pi/4} \sqrt{\pi \rho_{\pm}/(2v_{c,\pm} r)}$  with  $\rho_{\pm} = (4\pi^2 v_{c,\pm} \kappa_{\pm})^{-1}$ . Here, to account for  $\pm \mathbf{r}$ , we define  $k_{c,\pm} = k_{x,c}(\theta_{\pm \mathbf{r}}) \cos \theta_{\pm \mathbf{r}} + k_{y,c}(\theta_{\pm \mathbf{r}}) \sin \theta_{\pm \mathbf{r}}$ ,  $\mathbf{v}_{c,\pm} = \mathbf{v}_c(\pm \mathbf{r})$ ,  $\kappa_{\pm} = \kappa(\theta_{\pm \mathbf{r}})$ , and  $\Theta_{\pm} = \Theta_{\mathbf{k}_{c,\pm}}$ . To arrive at the explicit expression of the GF, the QPI in real space can be derived conveniently by incorporating a magnetic impurity potential [17,18,47], precise STM measurements were used to extract information on the electronic structure of the host system.

To describe the imperfection as a  $\delta$ -function potential  $\mathbf{V}_{\alpha} \delta(\mathbf{r})$  with  $\mathbf{V}_{\alpha} = \mathcal{V} \sigma_{\alpha}$ ,  $\delta Q_{\alpha\beta}(\varepsilon, \mathbf{r})$  would have an explicit form in the Born approximation [42]. In realistic measurements, we anticipate that the introduced magnetic impurity would have a weak influence on the TISS, making Born approximation reasonable. To adopt  $\mathbf{V}_{\alpha} = \mathcal{V} \sigma_z$ , we obtain

$$\delta Q_{z0} \approx \delta Q_{a,z0} \sin(k_+ r), \quad \delta Q_{a,z0} \equiv \mathcal{C} \sin(\Theta_- - \Theta_+), \quad (8a)$$

$$\delta Q_{zx} \approx \delta Q_{a,zx} \sin(k_+ r), \quad \delta Q_{a,zx} \equiv \mathcal{C} (\sin \Theta_- - \sin \Theta_+), \quad (8b)$$

$$\delta Q_{zy} \approx \delta Q_{a,zy} \sin(k_+ r), \quad \delta Q_{a,zy} \equiv C(\cos \Theta_+ - \cos \Theta_-), \quad (8c)$$

$$\delta Q_{zz} \approx \delta Q_{a,zz} \cos(k_+ r), \quad \delta Q_{a,zz} \equiv C - C \cos(\Theta_- - \Theta_+), \quad (8d)$$

where  $C = -(\mathcal{V}/r)\sqrt{\rho_+\rho_-/(v_{c,+}v_{c,-})}$ ,  $k_+ = k_{c,+} + k_{c,-}$  and  $\delta Q_{a,z\beta}$  is the amplitude of  $\delta Q_{z\beta}$ . If one completes the measurement of the QPI in real space induced by the designed imperfection, it is convenient to compare with our theoretical simulations, which help determine the Hamiltonian parameters of  $v_F$  and  $\mathbf{t}$ , and then all physical quantities through the Hamiltonian, e.g., CEC and the group velocities  $v_{c,\pm}$ . This direct comparison based on the QPI in real space profits from Eq. (3) for the ultimate real-space GF. In particular, the magnetic impurity potential strength  $\mathcal{V}$  may first be extracted by performing an identical STM experiment at zero magnetic field because the Hamiltonian parameters are known. Unlike the conventional QPI in momentum space [7], the proposed QPI in real space [cf. Fig. 2(c)] is more intuitive.

The spin texture embodying the spinor phase of eigenstates is one of the most remarkable properties of the TISS, which is generally probed by angle-resolved photoemission spectroscopy (ARPES) [7,48,49]. However, ARPES is incompatible with magnetic fields [7]. To our knowledge, spin texture has not been measured experimentally using STM, although it is compatible with magnetic fields. Nontrivially, our explicit derivations favor the extraction of the momentum-resolved spin texture of the TISS under an in-plane magnetic field from the amplitudes of the QPI in real space:

$$C = \frac{\delta Q_{a,zx}^2 + \delta Q_{a,zy}^2}{2\delta Q_{a,zz}}, \quad (9a)$$

$$\cos(\Theta_+ - \Theta_-) = 1 - \frac{\delta Q_{a,zx}^2 + \delta Q_{a,zy}^2}{2C^2}, \quad (9b)$$

$$\cos(\Theta_+ + \Theta_-) = \frac{\delta Q_{a,zx}^2 - \delta Q_{a,zy}^2}{\delta Q_{a,zx}^2 + \delta Q_{a,zy}^2}. \quad (9c)$$

Therefore, the spinor phase information or the spin orientation  $\Theta_{\pm}$  of eigenstates on the stationary points  $\mathbf{k}_{c,\pm}$  can be solved. For the TISS, the QPI in real space should first be given, i.e.,  $\delta Q_{zx}$ ,  $\delta Q_{zy}$ , and  $\delta Q_{zz}$ , as shown in Figs. 3(a)–3(c). Along an arbitrary direction, one can extract the amplitudes  $\delta Q_{a,zx}$ ,  $\delta Q_{a,zy}$ , and  $\delta Q_{a,zz}$  [cf. the green lines in Figs. 3(d)–3(f)], which yields  $\Theta_{\pm}$  according to Eq. (9). Considering different directions, the spin texture, i.e.,  $\Theta_{\pm}$  as a function of  $\theta_v$  [cf. the black dotted lines in Figs. 4], is determined by considering different tilt vectors. Note that we use  $\delta Q_{a,zy} = 0$  for  $\theta_r = 0$  and  $\delta Q_{a,zx} = 0$  for  $\theta_r = \pi/2$  due to the faster  $1/r^2$  decay of  $\delta Q_{zy}$  and  $\delta Q_{zx}$ . When the numerical extraction is performed, the STM measurement simultaneously determines  $\Theta_{\pm}$  of two states related to each

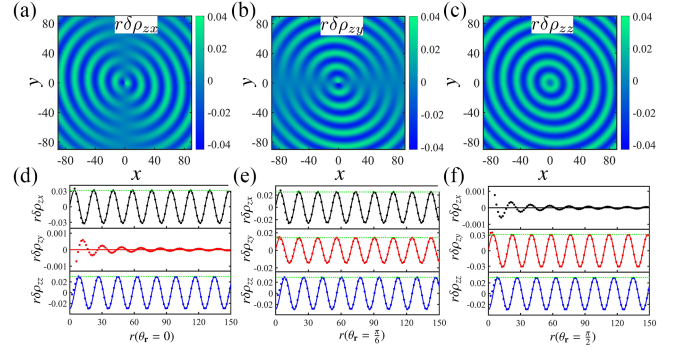


FIG. 3. (a)–(c) The calculated  $r\delta\rho_{zx}$ ,  $r\delta\rho_{zy}$ ,  $r\delta\rho_{zz}$ . (d)–(f) Along three directions,  $\theta_r = 0, \pi/6, \pi/2$ , the amplitudes  $r\delta\rho_{a,zx}$ ,  $r\delta\rho_{a,zy}$ ,  $r\delta\rho_{a,zz}$  of  $r\delta\rho_{zx}$ ,  $r\delta\rho_{zy}$ ,  $r\delta\rho_{zz}$  can be given (green lines). Here,  $t_x = t_y = 0.3v_F$ ,  $\mathcal{V} = 3$  eV, and  $\varepsilon = 0.15$  eV.

other through the backscattering event. For the known Hamiltonian parameters, the eigenstates can be calculated and then give the exact  $\Theta_{\pm}$  [cf. the red solid lines in Fig. 4]. For the TISS, the numerical construction of the spin texture, i.e., Eq. (9), does not require the input of information from the Hamiltonian except assuming a spin-1/2 model. As expected, the black and red lines in Fig. 4 agree well with each other. For the experiments, the measurable results should replace Fig. 3, and then Fig. 4 should be obtained using Eq. (9). The experimental data shown in Fig. 3 may be imperfect, which can be simulated by incorporating random numerical points. The difference from the theoretical  $\Theta_{\pm}$  is rather trivial when considering a 10% random amplitude perturbation [cf. the green dotted lines in the first and second columns in Fig. 4] when the tilt is moderately strong, and it becomes more significant when the tilt is enhanced [cf. the green dotted lines in the third column in Fig. 4] as anticipated.

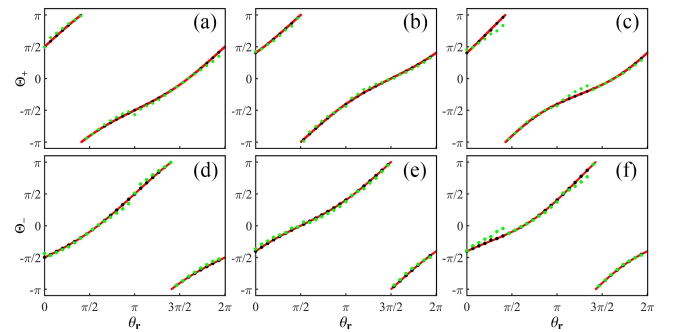


FIG. 4. The  $\Theta_+$  [top row, (a)–(c)] and  $\Theta_-$  [bottom row, (d)–(f)] extracted by utilizing Eq. (9) for the spinor phase of eigenstates or the spin texture. We use  $t_x = 0.3v_F$  and  $t_y = 0$ ,  $t_x = 0$  and  $t_y = 0.3v_F$ , and  $t_x = 0.3v_F$  and  $t_y = 0.3v_F$  for the first, second, and third columns, respectively. In each panel, there are three lines, i.e., the exact  $\Theta_+$  or  $\Theta_-$  from the eigenstates (red solid lines), and the numerical extraction by using Eq. (9) with random amplitude perturbation (black dotted lines for 0% and green dotted lines for 10%). Here,  $\mathcal{V} = 3$  eV, and  $\varepsilon = 0.15$  eV.

Our theoretical derivations should be evaluated further. In particular,  $\kappa_+ = \kappa_- \equiv \kappa_0$  for Eq. (1), so Eq. (9a) can also be used to directly determine the Riemann curvature because

$$C = -\frac{\mathcal{V}}{4\pi^2 r \kappa_0 v_{c,+} v_{c,-}}, \quad (10)$$

and  $v_{c,\pm}$  should be provided through the Hamiltonian construction as discussed previously. This provides a direct approach to resolving the local curvature of the CECs, unlike the *indirect* manner of QPI in momentum space which needs to obtain the CEC firstly.

*Experimental feasibility*—According to Fig. 2(c), the GDOS implies the extraction of the spinor phase of the eigenstates or the spin texture from the amplitudes of the spin-polarized STM measurements. This extraction requires impurity design and/or spin-polarized STM measurement similar to that for characterizing the Berry phase [17,18]. However, it is more intrinsic because the phase accumulation of spin vectors (underlying the spin texture) along a momentum loop yields the Berry phase [50–52]. This originates from the local (global) properties of the GDOS (Berry phase). In our proposal, both magnetic impurity and the STM probe should be considered as the atomic-scale leads. Both of these work in the linear response regime, i.e., it is appropriate to describe the magnetic impurity potential in the Born approximation [42] and the STM tip potential in the Tersoff-Hamman approximation [53]. If a controllable  $T$  matrix [cf. Eq. (5)] can be realized in an experiment, i.e., the orthogonal spin information is given as  $\sigma_{z\beta}$  with  $\beta = x, y, z$  for the  $\sigma_z$ -type impurity [cf. Eq. (8)], the proposed method does not constrain the impurity potential or the STM tip to be weak. In principle, a single impurity plus an STM probe is equivalent to two STM probes, so the dual-probe STM may be an alternative method to realize the proposed measurement of spin texture [54].

The magnetic doped topological insulator has attracted wide theoretical and experimental interest owing to its potential as a quantum anomalous Hall insulator [55,56]. Combined with the rapid experimental advances in spin-polarized STM technology [57–63], our proposal is likely to be verified in short term. After the spin texture measurement is realized experimentally, it is promising to characterize the Berry curvature [64–68] and even the quantum geometric tensor [69–73] through spin-polarized STM measurements.

*Conclusions*—In this study, we introduced a geometric amplitude to locally describe the electronic band structure, namely, the GDOS. The GDOS simplifies the construction of the real-space GF as the basis for local responses and makes it attain the ultimate expression with clear physics. In particular, the amplitude factor of the GF embodies the

spinor phase information of the eigenstates, which is utilized in QPI in real space to extract the spin texture of the TISS under an in-plane magnetic field. Therefore, the proposed GDOS deepens our understanding of electronic band structures and is indispensable in local responses, and it should be universal for any periodic system, such as photonic [74] and phononic crystals [75].

*Acknowledgments*—This work was supported by Innovation Program for Quantum Science and Technology (Grant No. 2024ZD0300104), the NSAF grant in NSFC with grant No. U2230402, and NSFC (Grants No. 12174019, No. 12274019, No. 12274411). S. H. Z. is also supported by the Fundamental Research Funds for the Central Universities (QNYC202402). We acknowledge the computational support provided by the Beijing Computational Science Research Center (CSRC) and Hefei Advanced Computing Center.

- 
- [1] C. Kittel, *Introduction to Solid State Physics*, 8th ed. (Wiley, New York, 2005).
  - [2] P. Törmä, *Phys. Rev. Lett.* **131**, 240001 (2023).
  - [3] M. V. Berry, *Proc. R. Soc. A* **392**, 45 (1984).
  - [4] E. Cohen, H. Larocque, F. Bouchard, F. Nejdassattari, Y. Gefen, and E. Karimi, *Nat. Rev. Phys.* **1**, 437 (2019).
  - [5] D. Xiao, M.-C. Chang, and Q. Niu, *Rev. Mod. Phys.* **82**, 1959 (2010).
  - [6] D. Vanderbilt, *Berry Phases in Electronic Structure Theory: Electric Polarization, Orbital Magnetization and Topological Insulators* (Cambridge University Press, Cambridge, England, 2018).
  - [7] J.-X. Yin, S. H. Pan, and M. Zahid Hasan, *Nat. Rev. Phys.* **3**, 249 (2021).
  - [8] C. Zhang, Z. Yi, and W. Xu, *Mater. Futures* **1**, 032301 (2022).
  - [9] A. H. Castro Neto, F. Guinea, N. M. R. Peres, K. S. Novoselov, and A. K. Geim, *Rev. Mod. Phys.* **81**, 109 (2009).
  - [10] W. Han, R. K. Kawakami, M. Gmitra, and J. Fabian, *Nat. Nanotechnol.* **9**, 794 (2014).
  - [11] R. Wang, X.-G. Ren, Z. Yan, L.-J. Jiang, W. E. I. Sha, and G.-C. Shan, *Front. Phys.* **14**, 13603 (2018).
  - [12] Y. Liu, N. O. Weiss, X. Duan, H.-C. Cheng, Y. Huang, and X. Duan, *Nat. Rev. Mater.* **1**, 16042 (2016).
  - [13] D. Akinwande, C. Huyghebaert, C.-H. Wang, M. I. Serna, S. Goossens, L.-J. Li, H.-S. P. Wong, and F. H. L. Koppens, *Nature (London)* **573**, 507 (2019).
  - [14] K. S. Novoselov, A. Mishchenko, A. Carvalho, and A. H. Castro Neto, *Science* **353**, aac9439 (2016).
  - [15] A. Avsar, H. Ochoa, F. Guinea, B. Özyilmaz, B. J. van Wees, and I. J. Vera-Marun, *Rev. Mod. Phys.* **92**, 021003 (2020).
  - [16] Y. Kohsaka, T. Machida, K. Iwaya, M. Kanou, T. Hanaguri, and T. Sasagawa, *Phys. Rev. B* **95**, 115307 (2017).
  - [17] C. Dutreix, H. Gonzalez-Herrero, I. Brihuega, M. I. Katsnelson, C. Chapelier, and V. T. Renard, *Nature (London)* **574**, 219 (2019).

- [18] Y. Zhang, Y. Su, and L. He, *Phys. Rev. Lett.* **125**, 116804 (2020).
- [19] S.-H. Zheng, H.-J. Duan, J.-K. Wang, J.-Y. Li, M.-X. Deng, and R.-Q. Wang, *Phys. Rev. B* **101**, 041408(R) (2020).
- [20] W. Rao, Y.-L. Zhou, Y.-j. Wu, H.-J. Duan, M.-X. Deng, and R.-Q. Wang, *Phys. Rev. B* **103**, 155415 (2021).
- [21] S.-B. Zhang, C.-A. Li, F. Peña Benitez, P. Surówka, R. Moessner, L. W. Molenkamp, and B. Trauzettel, *Phys. Rev. Lett.* **127**, 076601 (2021).
- [22] A. Thenappambil, G.E. dos Santos, C.-A. Li, M. Abdelghany, W. Beugeling, H. Buhmann, C. Gould, S.-B. Zhang, B. Trauzettel, and L. W. Molenkamp, *Nano Lett.* **23**, 6914 (2023).
- [23] See Supplemental Material at <http://link.aps.org/supplemental/10.1103/PhysRevLett.133.036204> for derivation details on the Riemann or differential curvature of a curve, the ultimate real-space Green's function, an alternative way to obtain the geometric density of states, the Hamiltonian for the surface states on a three-dimensional topological insulator under an in-plane magnetic field and  $T$ -matrix approach, and the extraction of the spin texture of the Rashba two-dimensional electron gas from the amplitude of quasiparticle interference in real space, which includes Refs. [24–33].
- [24] S.-H. Zhang, D.-F. Shao, and W. Yang, *J. Magn. Magn. Mater.* **491**, 165631 (2019).
- [25] G.C. Paul, S.F. Islam, and A. Saha, *Phys. Rev. B* **99**, 155418 (2019).
- [26] L. M. Roth, H. J. Zeiger, and T. A. Kaplan, *Phys. Rev.* **149**, 519 (1966).
- [27] S. Lounis, P. Zahn, A. Weismann, M. Wenderoth, R. G. Ulbrich, I. Mertig, P.H. Dederichs, and S. Blügel, *Phys. Rev. B* **83**, 035427 (2011).
- [28] H. Zhang, C.-X. Liu, X.-L. Qi, X. Dai, Z. Fang, and S.-C. Zhang, *Nat. Phys.* **5**, 438 (2009).
- [29] W.-Y. Shan, H.-Z. Lu, and S.-Q. Shen, *New J. Phys.* **12**, 043048 (2010).
- [30] C.-X. Liu, X.-L. Qi, H. Zhang, X. Dai, Z. Fang, and S.-C. Zhang, *Phys. Rev. B* **82**, 045122 (2010).
- [31] A. A. Taskin, H. F. Legg, F. Yang, S. Sasaki, Y. Kanai, K. Matsumoto, A. Rosch, and Y. Ando, *Nat. Commun.* **8**, 1340 (2017).
- [32] D. Rakhmievich, F. Wang, W. Zhao, M. H. W. Chan, J. S. Moodera, C. Liu, and C.-Z. Chang, *Phys. Rev. B* **98**, 094404 (2018).
- [33] H. Imamura, P. Bruno, and Y. Utsumi, *Phys. Rev. B* **69**, 121303(R) (2004).
- [34] S.-H. Zhang, J.-J. Zhu, W. Yang, and K. Chang, *Phys. Rev. B* **99**, 195456 (2019).
- [35] M. Y. Toriyama, A. M. Ganose, M. Dylla, S. Anand, J. Park, M. K. Brod, J. M. Munro, K. A. Persson, A. Jain, and G. J. Snyder, *Mater. Today Electron.* **1**, 100002 (2022).
- [36] M. P. do Carmo, *Differential Geometry of Curves and Surfaces* (Dover Publications, New York, 2016).
- [37] E. N. Economou, *Green's Functions in Quantum Physics* (Springer, Berlin, 1983).
- [38] S.-H. Zhang, J.-J. Zhu, W. Yang, and K. Chang, *2D Mater.* **4**, 035005 (2017).
- [39] K. Zhao, Y.-F. Lv, S.-H. Ji, X. Ma, X. Chen, and Q.-K. Xue, *J. Phys. Condens. Matter* **26**, 394003 (2014).
- [40] N. Avraham, J. Reiner, A. Kumar-Nayak, N. Morali, R. Batabyal, B. Yan, and H. Beidenkopf, *Adv. Mater.* **30**, 1707628 (2018).
- [41] L. Chen, P. Cheng, and K. Wu, *J. Phys. Condens. Matter* **29**, 103001 (2017).
- [42] E. N. Economou, *Green's Functions in Quantum Physics*, 3rd ed. (Springer-Verlag, Berlin/Heidelberg, 2006).
- [43] R. R. Biswas and A. V. Balatsky, *Phys. Rev. B* **81**, 233405 (2010).
- [44] Q. Liu, X.-L. Qi, and S.-C. Zhang, *Phys. Rev. B* **85**, 125314 (2012).
- [45] M. Istas, C. Groth, and X. Waintal, *Phys. Rev. Res.* **1**, 033188 (2019).
- [46] S. Smidstrup, T. Markussen, P. Vancaeyveld, J. Wellendorff, J. Schneider, T. Gunst, B. Verstichel, D. Stradi, P. A. Khomyakov, U. G. Vej-Hansen *et al.*, *J. Phys. Condens. Matter* **32**, 015901 (2019).
- [47] H. González-Herrero, J. M. Gómez-Rodríguez, P. Mallet, M. Moaied, J. J. Palacios, C. Salgado, M. M. Ugeda, J.-Y. Veuillen, F. Yndurain, and I. Brihuega, *Science* **352**, 437 (2016).
- [48] D. Hsieh, Y. Xia, D. Qian, L. Wray, J. H. Dil, F. Meier, J. Osterwalder, L. Patthey, J. G. Checkelsky, N. P. Ong *et al.*, *Nature (London)* **460**, 1101 (2009).
- [49] D. Hsieh, Y. Xia, L. Wray, D. Qian, A. Pal, J. H. Dil, J. Osterwalder, F. Meier, G. Bihlmayer, C. L. Kane *et al.*, *Science* **323**, 919 (2009).
- [50] J. N. Fuchs, F. Piéchon, M. O. Goerbig, and G. Montambaux, *Eur. Phys. J. B* **77**, 351 (2010).
- [51] S.-H. Zhang, J. Yang, D.-F. Shao, Z. Wu, and W. Yang, *Phys. Rev. B* **103**, L161407 (2021).
- [52] J. Yang, D.-F. Shao, S.-H. Zhang, and W. Yang, *Phys. Rev. B* **104**, 035402 (2021).
- [53] J. Tersoff and D. R. Hamann, *Phys. Rev. B* **31**, 805 (1985).
- [54] T. Nakayama, O. Kubo, Y. Shingaya, S. Higuchi, T. Hasegawa, C.-S. Jiang, T. Okuda, Y. Kuwahara, K. Takami, and M. Aono, *Adv. Mater.* **24**, 1675 (2012).
- [55] Q. Liu, C.-X. Liu, C. Xu, X.-L. Qi, and S.-C. Zhang, *Phys. Rev. Lett.* **102**, 156603 (2009).
- [56] C.-Z. Chang, C.-X. Liu, and A. H. MacDonald, *Rev. Mod. Phys.* **95**, 011002 (2023).
- [57] G. A. Fiete and E. J. Heller, *Rev. Mod. Phys.* **75**, 933 (2003).
- [58] F. Meier, L. Zhou, J. Wiebe, and R. Wiesendanger, *Science* **320**, 82 (2008).
- [59] L. Zhou, J. Wiebe, S. Lounis, E. Vedmedenko, F. Meier, S. Blugel, P. H. Dederichs, and R. Wiesendanger, *Nat. Phys.* **6**, 187 (2010).
- [60] H. Oka, P. A. Ignatiev, S. Wedekind, G. Rodary, L. Niebergall, V. S. Stepanyuk, D. Sander, and J. Kirschner, *Science* **327**, 843 (2010).
- [61] K. Alexander Ako, W. Jens, C. Bruno, and W. Roland, *Science* **332**, 1062 (2011).

- [62] B. Verlhac, N. Bachellier, L. Garnier, M. Ormaza, P. Abufager, R. Robles, M.-L. Bocquet, M. Ternes, N. Lorente, and L. Limot, *Science* **366**, 623 (2019).
- [63] L. Schneider, P. Beck, J. Wiebe, and R. Wiesendanger, *Sci. Adv.* **7**, eabd7302 (2021).
- [64] N. Fläschner, B. S. Rem, M. Tarnowski, D. Vogel, D.-S. Lühmann, K. Sengstock, and C. Weitenberg, *Science* **352**, 1091 (2016).
- [65] M. Schüler, U. De Giovannini, H. Hübener, A. Rubio, M. A. Sentef, and P. Werner, *Sci. Adv.* **6**, 2730 (2020).
- [66] T. T. Luu and H. J. Wörner, *Nat. Commun.* **9**, 916 (2018).
- [67] M. Wimmer, H. M. Price, I. Carusotto, and U. Peschel, *Nat. Phys.* **13**, 545 (2017).
- [68] C. De Beule and E. J. Mele, *Phys. Rev. Lett.* **131**, 196603 (2023).
- [69] O. Bleu, D. D. Solnyshkov, and G. Malpuech, *Phys. Rev. B* **97**, 195422 (2018).
- [70] M. Yu, P. Yang, M. Gong, Q. Cao, Q. Lu, H. Liu, S. Zhang, M. B. Plenio, F. Jelezko, T. Ozawa *et al.*, *Natl. Sci. Rev.* **7**, 254 (2019).
- [71] X. Tan, D.-W. Zhang, Z. Yang, J. Chu, Y.-Q. Zhu, D. Li, X. Yang, S. Song, Z. Han, Z. Li *et al.*, *Phys. Rev. Lett.* **122**, 210401 (2019).
- [72] A. Gianfrate, O. Bleu, L. Dominici, V. Ardizzone, M. De Giorgi, D. Ballarini, G. Lerario, K. W. West, L. N. Pfeiffer, D. D. Solnyshkov *et al.*, *Nature (London)* **578**, 381 (2020).
- [73] J. Ren, Q. Liao, F. Li, Y. Li, O. Bleu, G. Malpuech, J. Yao, H. Fu, and D. Solnyshkov, *Nat. Commun.* **12**, 689 (2021).
- [74] T. Ozawa, H. M. Price, A. Amo, N. Goldman, M. Hafezi, L. Lu, M. C. Rechtsman, D. Schuster, J. Simon, O. Zilberberg *et al.*, *Rev. Mod. Phys.* **91**, 015006 (2019).
- [75] M.-H. Lu, L. Feng, and Y.-F. Chen, *Mater. Today* **12**, 34 (2009).